On the acoustic radiation of a pitching airfoil

A. Manela

Additional information on Phys. Fluids

On the acoustic radiation of a pitching airfoil

A. Manela

*Faculty of Aerospace Engineering, Technion – Israel Institute of Technology,
Haifa 32000, Israel*

We examine the acoustic far field of a thin elastic airfoil, immersed in low-Mach non-uniform stream flow, and actuated by small-amplitude sinusoidal pitching motion. The near-field fluid-structure interaction problem is analyzed using potential thin-airfoil theory, combined with a discrete vortex model to describe the evolution of airfoil trailing edge wake. The leading order dipole-sound signature of the system is investigated using Powell-Howe acoustic analogy. Compared with a pitching *rigid* airfoil, the results demonstrate a two-fold effect of structure elasticity on airfoil acoustic field: at actuation frequencies close to the system least stable eigenfrequency, elasticity amplifies airfoil motion amplitude and associated sound levels; however, at frequencies distant from this eigenfrequency, structure elasticity acts to absorb system kinetic energy and reduce acoustic radiation. In the latter case, and with increasing pitching frequency ω_p, a rigid-airfoil setup becomes significantly noisier than an elastic airfoil, owing to an $\omega_p^{5/2}$ increase of its direct motion noise component. Unlike rigid airfoil signature, it is shown that wake sound contribution to elastic airfoil radiation is significant for all ω_p. Remarkably, this contribution contains, in addition to the fundamental pitching frequency, its odd multiple harmonics, which result from nonlinear interactions between the airfoil and the wake. The results suggest that structure elasticity may serve as a viable means for design of flapping flight noise control methodologies. © *2013 AIP Publishing LLC*. [http://dx.doi.org/10.1063/1.4816295]

I. INTRODUCTION

Fluid-structure interactions, coupling the dynamics of thin elastic structures and ambient fluid flow, have recently become the focus of a large number of studies.[1,2] Motivated by a variety of natural and practical applications, these studies include investigations on flapping flag motion[3,4] and fish locomotion,[5] as well as examination of paper flutter in commercial printing machines[6] and design of novel green-energy methodologies for energy harvesting of oscillating filaments.[7] These and others have combined into a series of theoretical and experimental works, analyzing various aspects of near-field fluid-structure coupling phenomena and associated topics.

In parallel with studies on near-field interactions, consideration of far-field radiation from coupled fluid-structure systems has also become a topic of growing interest.[8] Yet, up until recently, these studies were focusing mainly on rigid-body configurations, thus reducing the level of complexity of problems involved by *prescribing* the dynamics of the structure. Increasing interest in sound production processes in elastic-body setups, such as during palatal snoring[9] and insect flight,[10–12] has enforced progress in the field of *vibroacoustics*, analyzing far-field noise radiation resulting from flow-induced body motions.

Early works on near-field thin-structure-fluid interactions have focused on determining the critical conditions and analyzing the supercritical behavior of a thin filament subject to uniform flow (e.g., Refs. 13–15). Later on, boundary actuation[16,17] and incoming flow non-uniformities[18,19] have been incorporated to investigate the dynamics of active flapping motion in uniform and non-uniform flows. Counterpart vibroacoustic studies have followed to consider both unforced[20] and forced[21–23] setups, and evaluate the associated acoustic far-field. Notably, when analyzing the effect of flow unsteadiness on near- and far-field dynamics, all of the above studies have applied various degrees

of approximation. Modeling flow unsteadiness as a prescribed distribution of incoming vorticity, Manela and Howe,[18] Alben,[19] and Manela[21] have considered a *linearized* regime, where incoming flow vorticity was weak enough so that it was convected with the mean flow. Specifically, the convected vorticity was unaffected by the presence of the structure or by the topology of trailing edge wake. Such an approximation effectively neglects any reaction of the solid body on fluid vortex dynamics, yet such reaction clearly exists for any finite strength of incoming vorticity. This approximation may be of particular significance in the context of sound-generation problems, where variations in vortical motions are known to have a key effect on the system far-field radiation.[8,24] When coupled with leading edge actuation, the nonlinear fluid-structure interaction problem, incorporating the full reciprocal reactions of body motion on unsteady flow dynamics, has not been considered.

In the few cases where flow vortex dynamics was analyzed, other simplifying assumptions were made. Thus, Abou-Hussein *et al.*[25] have studied the dynamics and sound radiation by a line vortex passing past a rigid airfoil, but neglected the impact of trailing edge wake on vortex trajectory. Similarly, Alben[26] considered the near-field interaction of a flexible filament and a point vortex but did not account for vorticity release due to filament trailing edge singularity. Recently, Manela and Huang[27] analyzed both incident vortex dynamics and trailing edge singularity for flow over an airfoil, but considered only a rigid setup of a flapped profile.

Following these studies, the objective of the present work is to investigate a more comprehensive model for flapping-flight noise generation, where boundary actuation and flow inhomogeneity are nonlinearly coupled with structure elasticity. By solving both near-field and far-field problems, we aim at gaining more insight into the effect of fluid-structure interaction on the acoustic characteristics of flapping flight and, in particular, clarify the role of elasticity on sound emission. The model problem to be studied consists of a thin elastic airfoil at high Reynolds (potential) low Mach flow, subject to both pitching actuation and incident line-vortex forcing. Both incident vortex and trailing edge wake dynamics are modeled, and their total impact on the system acoustic properties is investigated.

This paper is organized as follows. In Sec. II, the near-field (hydrodynamic) and far-field (acoustic) problems are formulated and analyzed. In Sec. III, numerical results are presented, and the separate and combined effects of pitching, elasticity, and vortex dynamics are discussed. Concluding comments are given in Sec. IV.

II. PROBLEM FORMULATION

A. Near-field theory

Schematic of the problem is given in Fig. 1(a). Consider a thin (zero thickness) elastic airfoil of chord $2a$ and position denoted by $\xi = \xi(x_1, t)$. The airfoil is subject to uniform mean flow of speed U in the x_1-direction. At time $t \geq 0$, small-amplitude leading edge pitching of the form

$$\left(\frac{\partial \xi}{\partial x_1} \right)_{x_1 = -a} = \bar{\varepsilon}_p \sin(\omega_p t) \tag{1}$$

is applied, where $\bar{\varepsilon}_p \ll 1$ and ω_p is the prescribed pitching frequency. During the same time, an incident line vortex of strength Γ is released and interacts with the airfoil. It is assumed (and later on verified) that airfoil deflection remains small at all times ($|\xi| \ll a$), so that the linearized model for airfoil motion can be applied. Given the small angles of attack considered, leading edge flow detachment is excluded, and fluid vorticity is allowed only at the incident vortex location and along a trailing edge wake. Assuming small mean-flow Mach number, we treat the near-field flow as incompressible and potential, and being affected by the localized distribution of vorticity. In what follows we analyze the airfoil dynamics and associated fluid motion. Linearized thin-airfoil theory is applied to study the near-field fluid-structure interaction problem. To evaluate the effect of wing elasticity, our findings are compared with those obtained for a rigid-airfoil setup, presented in Fig. 1(b). In this case, structure deflection is fully prescribed by the form of pitching actuation (1), yielding

$$[\xi(-a \leq x_1 \leq a, t)]_{\text{rigid}} = \bar{\varepsilon}_p (x_1 + a) \sin(\omega_p t). \tag{2}$$
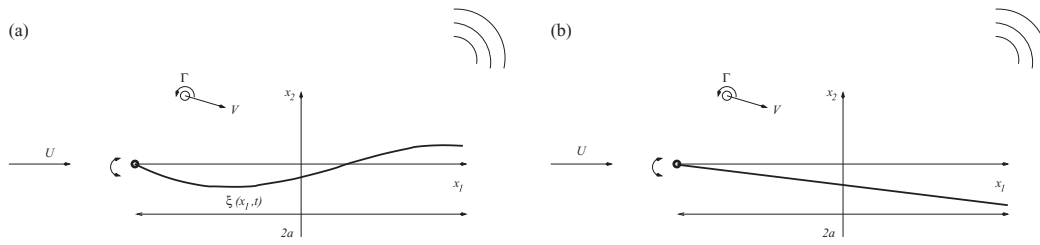
FIG. 1. Schematic of the (a) elastic and (b) rigid vortex-airfoil setups considered. In both cases, a thin airfoil is subject to sinusoidal leading edge pitching, uniform mean flow of speed U in the x_1-direction, and a passing line vortex of strength Γ.

We formulate an initial value problem, where at $t = 0$ the airfoil is aligned with the x_1-axis ($\xi = 0$), the incident vortex Γ is set into the flow, and leading edge actuation is commenced. The initial vortex location is chosen sufficiently upstream of the airfoil (see Sec. II C) to approximate a case where the vortex initially has a negligible impact on the near-field dynamics. In the following, we denote the instantaneous vortex location and velocity by $\mathbf{x}_\Gamma(t)$ and $\mathbf{v}_\Gamma(t) = \mathrm{d}\mathbf{x}_\Gamma/\mathrm{d}t$, respectively.

In accordance with potential thin-airfoil theory, the vortex interaction with structure end points induces square-root singularities in the flow field at the airfoil leading and trailing edges. Trailing edge singularity is regularized by application of the unsteady Kutta condition, which results in additional release of vorticity at the airfoil trailing edge. We model the production of trailing edge vorticity through the Brown and Michael equation,[28,29] which has been applied frequently to approximate high Reynolds number vortex shedding from two-dimensional setups, both in studies of near-field dynamics[15,16,30] and sound emission[31,32] problems. According to this model, shedding of vorticity is discretized into a sequence of concentrated line vortices whose position and strength vary with time. At a given time, one vortex is being shed from the airfoil trailing edge, in the form of a thin connecting sheet of infinitesimal circulation ending in a concentrated core of finite circulation Γ_n. The core strength changes with time according to the Kutta condition, while its position $\mathbf{x}_{\Gamma_n}$ is governed by the Brown and Michael[28,29] formula. When the time derivative $\mathrm{d}\Gamma_n/\mathrm{d}t$ changes sign, the vortex is detached from the thin sheet and propagates as a "free" line vortex with "frozen" (fixed) circulation. Simultaneously, the shedding of the next vortex, Γ_{n+1}, is initiated.

A shortcoming in the Brown and Michael model has been indicated by several authors (e.g., Refs. 33 and 34). Specifically, it was found that a spurious dipole is induced when using the original formulation, resulting from the time dependence of the circulation of the growing vortex. Consequently, corrections to the formula have been proposed to account for vortex shedding phenomena in stationary-structure systems. Yet, usage of any of these formulas in the present study would not be consistent with the moving-body setup considered. Instead, we formulate the problem in terms of the original equation. In a previous study of a non-stationary flapped-airfoil setup,[27] a comparison has been made between the predictions of the original and Howe's emended form[34] of the formula. The analysis has indicated that only small quantitative differences appear between the results. We therefore expect that no qualitative effects should occur due to the present use of the original equation, which is still considered a common model for describing vortex shedding phenomena from rigid- and elastic-structure configurations, for both near-field[15,16,30] and acoustic[31,32] investigations.

Making use of thin-airfoil methodology, the airfoil is represented by distribution of circulation $\gamma_a(x_1, t)$ ($-a \le x_1 \le a$) per unit length. To specify $\gamma_a(x_1, t)$, a no-penetration condition on the structure is imposed. In complex-variable notation, this condition is given by

$$\frac{\partial \xi}{\partial t} + U \frac{\partial \xi}{\partial x_1} = \mathrm{Im}\left\{\frac{\mathrm{i}}{2\pi}\left[\fint_{-a}^{a} \frac{\gamma_a(s,t)\mathrm{d}s}{x_1 - s} + \frac{\Gamma}{x_1 - z_\Gamma} + \sum_{k=1}^{n} \frac{\Gamma_k}{x_1 - z_{\Gamma_k}}\right]\right\}, \qquad (3)$$

where $z = x_1 + \mathrm{i}x_2$ is a complex representation of a point in the plane of motion, and z_Γ and z_{Γ_k} mark locations of incident and kth trailing edge vortices, respectively. The barred integral sign denotes a

principal value integral. The airfoil displacement $\xi(x_1, t)$ is governed by the linearized equation

$$\rho_s \frac{\partial^2 \xi}{\partial t^2} + EI \frac{\partial^4 \xi}{\partial x_1^4} = \Delta p(x_1, t), \tag{4}$$

balancing structure inertia, bending stiffness, and fluid loading terms. In (4), ρ_s marks airfoil mass per unit area, and EI denotes structure bending stiffness. On the right-hand side, $\Delta p = p_- - p_+$ marks fluid pressure jump between airfoil lower (p_-) and upper (p_+) surfaces. Making use of Bernoulli's equation, Δp is related to $\gamma_a(x_1, t)$ through

$$\Delta p(x_1, t) = -\rho_0 \left(\frac{\partial}{\partial t} \int_{-a}^{x_1} \gamma_a(s, t) \mathrm{d}s + U \gamma_a(x_1, t) \right), \tag{5}$$

where ρ_0 denotes the mean fluid density.

Equations (3)–(5) are coupled to the incident and trailing edge vortices dynamics through the right-hand side of Eq. (3). The motion of the incident vortex Γ is governed by

$$\frac{\mathrm{d}z_\Gamma}{\mathrm{d}t} = W_\Gamma^*, \tag{6}$$

where an asterisk marks the complex conjugate of a complex number, and

$$W_\Gamma = U - \frac{\mathrm{i}}{2\pi} \left(\int_{-a}^{a} \frac{\gamma_a(x_1, t) \mathrm{d}x_1}{z_\Gamma - x_1} + \sum_{k=1}^{n} \frac{\Gamma_k}{z_\Gamma - z_{\Gamma_k}} \right) \tag{7}$$

is the conjugate velocity induced at the instantaneous vortex location, after removing its self-singularity. Similarly, motions of the $\Gamma_1, \ldots, \Gamma_{n-1}$ "frozen" trailing edge vortices are governed by

$$\frac{\mathrm{d}z_{\Gamma_k}}{\mathrm{d}t} = W_{\Gamma_k}^*, \tag{8}$$

with $k = 1, \ldots, n - 1$, and

$$W_{\Gamma_k} = U - \frac{\mathrm{i}}{2\pi} \left(\int_{-a}^{a} \frac{\gamma_a(x_1, t) \mathrm{d}x_1}{z_{\Gamma_k} - x_1} + \sum_{\substack{m=1 \\ m \neq k}}^{n} \frac{\Gamma_m}{z_{\Gamma_k} - z_{\Gamma_m}} + \frac{\Gamma}{z_{\Gamma_k} - z_\Gamma} \right). \tag{9}$$

Following the above discussion, the time-varying strength and position of the nth trailing edge vortex are governed by the Brown and Michael equation,[28,29] which takes the form

$$\frac{\mathrm{d}z_{\Gamma_n}}{\mathrm{d}t} + (z_{\Gamma_n} - z_{\mathrm{TE}}) \frac{1}{\Gamma_n} \frac{\mathrm{d}\Gamma_n}{\mathrm{d}t} = W_{\Gamma_n}^*. \tag{10}$$

In addition, we impose the Kelvin theorem

$$\Gamma_n(t) = - \int_{-a}^{a} \gamma_a(x_1, t) \mathrm{d}x_1 - \sum_{k=1}^{n-1} \Gamma_k, \tag{11}$$

ensuring that the total system circulation (excluding the incident vortex) vanishes at all times. In (10), $W_{\Gamma_n}^*$ is given by Eq. (9) with $k = n$, and z_{TE} marks the complex-variable location of the trailing edge.

The nonlinear system of Eqs. (3)–(11) is solved in conjunction with an initial condition for the vortex location

$$z_\Gamma(t = 0) = z_{\Gamma_0}, \tag{12}$$

together with boundary conditions on the airfoil end points. Considering leading edge actuation of the form (1) and free-end conditions at $x_1 = a$, the boundary conditions applied at the airfoil

upstream and downstream ends are

$$\xi(-a, t) = 0 \,, \quad \left(\frac{\partial \xi}{\partial x_1}\right)_{(-a,t)} = \bar{\varepsilon}_p \sin(\omega t) \,, \quad \left(\frac{\partial^2 \xi}{\partial x_1^2}\right)_{(a,t)} = \left(\frac{\partial^3 \xi}{\partial x_1^3}\right)_{(a,t)} = 0. \tag{13}$$

The formulation of the near-field dynamical problem is completed by imposing the unsteady Kutta condition,

$$\gamma_a(a, t) = 0, \tag{14}$$

requiring that the fluid velocity at the trailing edge is finite. We assume that the release of the first trailing edge vortex starts at $t = 0$; the system evolution is then followed for $t > 0$ via numerical integration. Details regarding the numerical procedure and problem scaling are given in Sec. II C.

B. Far-field acoustic radiation

In the present small-amplitude, low-Mach, high-Reynolds-number flow setup, the far-field ($|\mathbf{x}| \to \infty$) acoustic pressure is governed by the Powell-Howe acoustic analogy,[8, 24]

$$\left(\frac{1}{c_0^2}\frac{\partial^2}{\partial t^2} - \nabla^2\right) p = \rho_0 \frac{\partial^2 \xi}{\partial t^2}\delta(x_2) + \rho_0 \nabla \cdot (\mathbf{\Omega} \times \mathbf{V}) \,, \tag{15}$$

where c_0 is the speed of sound, δ is the Dirac delta function, $\mathbf{V}$ is the fluid velocity, and $\mathbf{\Omega}$ is the vector of fluid vorticity. The latter is given by the sum of

$$\mathbf{\Omega}_\Gamma = \hat{\mathbf{x}}_\mathbf{3}\Gamma\delta(\mathbf{x} - \mathbf{x}_\Gamma(t)) \quad \text{and} \quad \mathbf{\Omega}_w = \sum_{k=1}^n \mathbf{\Omega}_{\Gamma_k} = \hat{\mathbf{x}}_\mathbf{3}\sum_{k=1}^n \Gamma_k\delta(\mathbf{x} - \mathbf{x}_{\Gamma_\mathbf{k}}(t)), \tag{16}$$

which mark the incident and trailing edge wake vorticities, respectively. Combining Eqs. (15) and (16), the acoustic pressure can be decomposed into a sum of "airfoil motion," "incident vortex," and "wake" contributions,

$$p(\mathbf{x}, t) = p_\xi(\mathbf{x}, t) + p_\Gamma(\mathbf{x}, t) + p_w(\mathbf{x}, t), \tag{17}$$

where

$$p_\xi(\mathbf{x}, t) = \rho_0 \frac{\partial}{\partial t}\int_0^\infty \frac{\partial \xi}{\partial \tau}\oint_{\mathcal{S}_\xi} G(\mathbf{x}, \mathbf{y}, t - \tau)\mathrm{d}S(\mathbf{y})\mathrm{d}\tau, \tag{18}$$

$$p_\Gamma(\mathbf{x}, t) = -\rho_0\int_0^\infty \int_{\mathcal{V}_\Gamma} (\mathbf{\Omega}_\Gamma \times \mathbf{V}_\Gamma)\cdot\frac{\partial G}{\partial \mathbf{y}}(\mathbf{x}, \mathbf{y}, t - \tau)\mathrm{d}\mathbf{y}\mathrm{d}\tau, \tag{19}$$

and

$$p_w(\mathbf{x}, t) = -\rho_0\sum_{k=1}^n\int_0^\infty \int_{\mathcal{V}_{\Gamma_k}} (\mathbf{\Omega}_{\Gamma_k} \times \mathbf{V}_{\Gamma_k})\cdot\frac{\partial G}{\partial \mathbf{y}}(\mathbf{x}, \mathbf{y}, t - \tau)\mathrm{d}\mathbf{y}\mathrm{d}\tau. \tag{20}$$

In (18)–(20), $\mathcal{S}_\xi$ is the airfoil surface, $\mathcal{V}_\Gamma$ and $\mathcal{V}_{\Gamma_k}$ denote the fluid regions occupied by the incident and trailing edge vortices, respectively, $G(\mathbf{x}, \mathbf{y}, t - \tau)$ is the acoustic Green's function having a vanishing normal derivative on the undisturbed airfoil, and $\mathbf{V}_\Gamma$ and $\mathbf{V}_{\Gamma_k}$ are the velocities of incident and trailing edge vortices, respectively.

We consider a case where the airfoil is acoustically compact, in which the acoustic wavelength is much larger than the airfoil chord. This is equivalent to the small-Mach assumption set for using Eq. (15).[24] Consequently, we apply the far-field two-dimensional compact Green's function,[24]

$$G(\mathbf{x}, \mathbf{y}, t - \tau) \approx \frac{\mathbf{x}\cdot\mathbf{Y}}{2\pi\sqrt{2c_0|\mathbf{x}|}}\frac{\partial}{\partial t}\left\{\frac{H(t_r - \tau)}{\sqrt{t_r - \tau}}\right\} \,, \quad |\mathbf{x}| \to \infty \,, \tag{21}$$

where $\mathbf{Y}(\mathbf{y})$ marks the *Kirchhoff* vector for the airfoil, and $t_r = t - |\mathbf{x}|/c_0$ is the *acoustic retarded time*. We approximate $\mathbf{Y}(\mathbf{y})$ by the Kirchhoff vector for an infinite strip,

$$\mathbf{Y}(\mathbf{y}) = \left(y_1, \ \mathrm{Re}\left\{ -\mathrm{i}\sqrt{(y_1 + \mathrm{i}y_2)^2 - a^2} \right\} \right). \tag{22}$$

Starting with the evaluation of $p_\xi(\mathbf{x}, t)$, substitute (21) into (18) to yield

$$p_\xi(\mathbf{x}, t) \approx \frac{\rho_0 \cos\theta}{\pi \sqrt{2c_0|\mathbf{x}|}} \frac{\partial^2}{\partial t^2} \int_0^{t_r} \frac{\mathrm{d}\tau}{\sqrt{t_r - \tau}} \int_{-a}^{a} \sqrt{a^2 - y_1^2} \frac{\partial \xi}{\partial \tau}(y_1, \tau)\, \mathrm{d}y_1, \tag{23}$$

where $\cos\theta = x_2/|\mathbf{x}|$ indicates the observer direction. In the simplified case of a *rigid* pitching airfoil depicted in Fig. 1(b),

$$[\partial\xi/\partial t]_{\mathrm{rigid}} = \bar{\varepsilon}_p \omega_p (x_1 + a) \cos(\omega_p t)$$

(see (2)), and the integral expression in (23) can be calculated explicitly for long times, yielding

$$[p_\xi(\mathbf{x}, t)]_{\mathrm{rigid}} \approx -\frac{\sqrt{\pi}\rho_0 a^3 \cos\theta}{4\sqrt{c_0|\mathbf{x}|}} \bar{\varepsilon}_p \omega_p^{5/2} \left[\cos(\omega_p t_r) + \sin(\omega_p t_r) \right], \ t_r \gg \omega_p^{-1}. \tag{24}$$

The long time limit in (24) is required for calculation of the time integral, and becomes valid, in practice, already after few pitching periods of the airfoil.

To evaluate p_Γ, substitute (21) together with (16) into (19) to obtain

$$p_\Gamma(\mathbf{x}, t) \approx \frac{\rho_0 \Gamma \sin\theta}{2\pi \sqrt{2c_0|\mathbf{x}|}} \frac{\partial}{\partial t} \int_0^{t_r} \frac{V_\Gamma^{(2)}(\tau)\mathrm{d}\tau}{\sqrt{t_r - \tau}}$$
$$- \frac{\rho_0 \Gamma \cos\theta}{2\pi \sqrt{2c_0|\mathbf{x}|}} \frac{\partial}{\partial t} \int_0^{t_r} \left(V_\Gamma^{(1)}(\tau)\frac{\partial Y_2}{\partial y_2} - V_\Gamma^{(2)}(\tau)\frac{\partial Y_2}{\partial y_1} \right)_{\mathbf{x}_\Gamma(\tau)} \frac{\mathrm{d}\tau}{\sqrt{t_r - \tau}}, \tag{25}$$

where $V_\Gamma^{(j)}$ denotes the velocity component of the incident vortex in the x_j-direction. Similarly, p_w is evaluated by substituting (16) and (21) into (20), to yield

$$p_w(\mathbf{x}, t) \approx \sum_{k=1}^{n} \left(\frac{\rho_0 \Gamma_k \sin\theta}{2\pi \sqrt{2c_0|\mathbf{x}|}} \frac{\partial}{\partial t} \int_0^{t_r} \frac{V_{\Gamma_k}^{(2)}(\tau)\mathrm{d}\tau}{\sqrt{t_r - \tau}} \right.$$
$$\left. - \frac{\rho_0 \Gamma_k \cos\theta}{2\pi \sqrt{2c_0|\mathbf{x}|}} \frac{\partial}{\partial t} \int_0^{t_r} \left(V_{\Gamma_k}^{(1)}(\tau)\frac{\partial Y_2}{\partial y_2} - V_{\Gamma_k}^{(2)}(\tau)\frac{\partial Y_2}{\partial y_1} \right)_{\mathbf{x}_{\Gamma_k}(\tau)} \frac{\mathrm{d}\tau}{\sqrt{t_r - \tau}} \right), \tag{26}$$

where $V_{\Gamma_k}^{(j)}$ marks the x_j-velocity component of the vortex Γ_k. In general, expressions (23), (25), and (26) for the pressure components are calculated numerically, based on the near-field solution of the problem formulated in Sec. II A. In addition to the "lift-type" dipole found for p_ξ in (23) (proportional to $\cos\theta$, therefore directed along the x_2-axis), both incident vortex and wake dipoles (25) and (26) have a "suction-type" component oriented along the mean-flow x_1-direction (proportional to $\sin\theta$). This component results directly from nonlinear vortex-airfoil interactions, leading to motions of the incident and trailing edge vortices in the normal x_2-direction. A similar finding was observed in previous studies considering sound radiation from nonlinear vortex interactions with rigid-wing setups.[25]

Typically, our calculations indicate that the suction pressure component is smaller than the lift component at all times. We therefore focus in our results on the lift dipole contribution. Here, as well, vortices motion in the normal direction affect the acoustic signal through the respective $V^{(2)}$ contributions to the second lines in (25) and (26). In addition, time variations in $V^{(1)}$ (which differs from the mean flow velocity U, particularly at times when the vortex passes in the vicinity of the airfoil) also affect the acoustic signal. These effects have not been incorporated in previous analyses of linearized fluid-structure interaction systems.[21,22]

C. Numerical procedure

Before proceeding to the presentation of results, the dimensional problem formulated in Secs. II A and II B should be non-dimensionalized. Towards this end, the length, velocity, time, frequency, and pressure are scaled by a, U, a/U, U/a, and $\rho_0 U^2$, respectively. The normalized form of the airfoil equation of motion (4) becomes

$$\frac{\partial^2 \bar{\xi}}{\partial \bar{t}^2} + \frac{1}{\bar{\alpha}^2} \frac{\partial^4 \bar{\xi}}{\partial \bar{x}_1^4} = \frac{1}{\bar{\mu}} \Delta \bar{p}, \tag{27}$$

where non-dimensional quantities are marked by overbars. Equation (27) is governed by the parameters

$$\bar{\mu} = \frac{\rho_s}{\rho a} \quad \text{and} \quad \bar{\alpha} = U \sqrt{\frac{\rho_s a^2}{EI}}, \tag{28}$$

denoting airfoil to fluid mass ratio and fluid to bending speed ratio (with bending speed given by $U_b = \sqrt{EI/\rho_s a^2}$), respectively. Omitting the presentation of the full non-dimensional problem for brevity, we note that the scaled dynamical problem is also governed by

$$\bar{\varepsilon}_p, \; \bar{\omega}_p = \frac{a}{U}\omega_p, \; \bar{\Gamma} = \frac{\Gamma}{2\pi a U}, \quad \text{and} \quad \bar{z}_{\Gamma_0} = \frac{z_{\Gamma_0}}{a}, \tag{29}$$

specifying the scaled pitching amplitude and frequency, and incident vortex circulation and initial location, respectively. To illustrate our results, we focus on a case where the incident vortex circulation is $\bar{\Gamma} = 0.2$. The vortex is initially located at $\bar{z}_{\Gamma_0} = -50 + 0.2i$, sufficiently far upstream of the airfoil, where it is essentially unaffected by the airfoil and convects along a straight line with the mean flow. In addition, we fix $\bar{\varepsilon}_p = 0.01$ (or otherwise consider the case $\bar{\varepsilon}_p = 0$ for reference; see Sec. III A), in accordance with the small-amplitude assumption set in Sec. II A.

The homogeneous (unforced) problem in the absence of incoming flow vorticity and leading edge actuation has been studied in Ref. 15, based on the Brown and Michael model.[28,29] In this work, the critical condition (namely, the neutral curve) for the onset of spontaneous structure motion has been delineated, in terms of combinations of $\bar{\mu}$ and $\bar{\alpha}$. To ensure that our small-amplitude assumption is satisfied, we focus here on a subcritical case, where the unperturbed airfoil state is stable. Specifically, we fix $\bar{\mu} = 10$ and $\bar{\alpha} = 1$, corresponding to $M^* = 0.2$ and $U^* = 2$ defined in Ref. 15 (cf. Fig. 4(a) therein). Our numerical calculations indicate that no significant differences are observed when choosing other subcritical $(\bar{\mu}, \bar{\alpha})$ combinations, and we therefore consider the present choice as representative for system response at subcritical conditions. With all the above quantities being specified, the only remaining free parameter is the pitching frequency $\bar{\omega}_p$, whose effect is studied below.

Numerical solution of the dynamical problem requires discretization of the system of equations in both space (along the airfoil chord) and time (from $t = 0$ to some final time). Space discretization is needed to express the vorticity distribution $\gamma_a(x_1, t)$ along the airfoil and the x_1-derivatives in the structure equation of motion. The numerical solution for $\bar{\gamma}_a(x_1, t)$ is obtained, in a standard procedure described in Ref. 27, via expansion of $\bar{\gamma}_a$ in a Fourier-type series (which satisfies the Kutta condition (14) identically) and truncation. The system of equations is integrated in time using a fourth-order Runge-Kutta algorithm. The typical time step used for integration was $\pi/2000\bar{\omega}_p$ (but not smaller than $\pi/2000$ for $\bar{\omega}_p < 1$), which proved sufficient for convergence (with errors $\lesssim 0.1\%$). Close to leading- and trailing-edge times (i.e., times when the vortex passes above the airfoil leading and trailing edges, respectively) smaller time steps ($\approx \pi/5000\bar{\omega}_p$, and not smaller than $\pi/5000$ for $\bar{\omega}_p < 1$) were required for convergence. This is because at these time instants the time scales for dynamic and acoustic signal variations are considerably smaller.

Adopting the scaling introduced, the non-dimensional form of the acoustic pressure (17) is

$$\frac{p(\mathbf{x}, t)}{\rho_0 U^2} = \sqrt{\frac{M}{8|\bar{\mathbf{x}}|}} \Pi_{\text{tot}}(\bar{t}_r) = \sqrt{\frac{M}{8|\bar{\mathbf{x}}|}} \left(\Pi_\xi(\bar{t}_r) + \Pi_\Gamma(\bar{t}_r) + \Pi_w(\bar{t}_r) \right), \tag{30}$$

where

$$\Pi_\xi(\bar{t}_r) \approx \frac{2}{\pi} \cos\theta \frac{\partial^2}{\partial \bar{t}^2} \int_0^{\bar{t}_r} \frac{d\tau}{\sqrt{\bar{t}_r - \tau}} d\tau \int_{-1}^1 \sqrt{1 - y_1^2} \frac{\partial \bar{\xi}}{\partial \tau}(y_1, \tau) \, dy_1, \tag{31}$$

$$\Pi_\Gamma(\bar{t}_r) \approx 2\bar{\Gamma} \left[\sin\theta \frac{\partial}{\partial \bar{t}} \int_0^{\bar{t}_r} \frac{\bar{V}_\Gamma^{(2)} d\tau}{\sqrt{\bar{t}_r - \tau}} - \cos\theta \frac{\partial}{\partial \bar{t}} \int_0^{\bar{t}_r} \mathrm{Re} \left\{ \frac{\left(\bar{V}_\Gamma^{(1)} + \mathrm{i}\bar{V}_\Gamma^{(2)}\right) \bar{z}_\Gamma d\tau}{\sqrt{(\bar{z}_\Gamma^2 - 1)(\bar{t}_r - \tau)}} \right\} \right], \tag{32}$$

and

$$\Pi_w(\bar{t}_r) \approx \sum_{k=1}^n \bar{2}\Gamma_k \left[\sin\theta \frac{\partial}{\partial \bar{t}} \int_0^{\bar{t}_r} \frac{\bar{V}_{\Gamma_k}^{(2)} d\tau}{\sqrt{\bar{t}_r - \tau}} - \cos\theta \frac{\partial}{\partial \bar{t}} \int_0^{\bar{t}_r} \mathrm{Re} \left\{ \frac{\left(\bar{V}_{\Gamma_k}^{(1)} + \mathrm{i}\bar{V}_{\Gamma_k}^{(2)}\right) \bar{z}_{\Gamma_k} d\tau}{\sqrt{(\bar{z}_{\Gamma_k}^2 - 1)(\bar{t}_r - \tau)}} \right\} \right]. \tag{33}$$

In (33), $\bar{\Gamma}_k = \Gamma_k/(2\pi a U)$. The "rigid airfoil" counterpart of Π_ξ in (31) (see (24)) is

$$\left[\Pi_\xi(\bar{t}_r)\right]_{\mathrm{rigid}} \approx -\sqrt{\frac{\pi}{2}} \cos\theta \, \bar{\varepsilon}_p \bar{\omega}_p^{5/2} \left(\cos(\bar{\omega}_p \bar{t}_r) + \sin(\bar{\omega}_p \bar{t}_r)\right), \quad \bar{t}_r \gg \bar{\omega}_p^{-1}. \tag{34}$$

Results for the acoustic pressure will be presented in terms of the acoustic "kernels" Π_{tot}, Π_f, Π_Γ, and Π_w. In addition to the parameters given by (28) and (29), the non-dimensional acoustic pressure is governed by the observer direction $\theta = \cos^{-1}(x_2/|\mathbf{x}|)$.

III. RESULTS

A. Non-pitching airfoil

For easy reference, we start by considering the case of a non-actuated airfoil (that is, $\bar{\varepsilon}_p = 0$), and compare between system responses for elastic and rigid airfoil configurations. Figure 2 describes the near-field dynamics for both elastic and rigid structure setups, presenting time evolutions of airfoil displacement (Fig. 2(a)) and total airfoil circulation (Fig. 2(b)), as well as instantaneous time snapshots of vortical flow field in the elastic (Fig. 2(c)) and rigid (Fig. 2(d)) setups. The total airfoil circulation presented in Fig. 2(b) is given by

$$\frac{\Gamma_a}{aU} = \int_{-1}^1 \frac{\gamma_a(\bar{x}_1, \bar{t})}{U} d\bar{x}_1 = -\sum_{k=1}^n \frac{\Gamma_k}{aU}, \tag{35}$$

in accordance with Kelvin's theorem (11). In agreement with the small amplitude of motion assumed for the analysis in Sec. II, $|\xi| \ll 1$ at all times.

Focusing on the system behavior at early times (prior to the incident vortex passage above the airfoil), we observe that, in the elastic case, the airfoil bends slightly upwards as the vortex approaches the structure (see the solid and dotted curves in Fig. 2(a), marking trailing edge (ξ_{TE}/a) and mid-chord ($\xi(x_1 = 0)/a$) displacements, respectively). This is in accordance with the counterclockwise velocity field induced by the vortex. At this stage, the differences between the total circulations of the elastic and rigid airfoils are minor (cf. the solid and dashed curves in Fig. 2(b) for $Ut/a < 40$). Yet, as the vortex approaches the airfoil leading edge and passes above it (at the time instant indicated by the left dashed-dotted lines in Figs. 2(a) and 2(b)), considerable airfoil displacements are observed in the elastic case, followed by large variations in the total circulation. Notably, vortex passage above the elastic airfoil induces oscillatory structure motion at a distinct frequency, reflected also through oscillatory variations in airfoil circulation (see the solid line in Fig. 2(b) for $Ut/a > 50$). The characteristics of elastic airfoil oscillations will be discussed below (see Fig. 4).

Apart from affecting structure dynamics, airfoil elasticity results in the release of alternate-sign "vortex street" vortices at times after incident vortex passage above the airfoil, as seen in Fig. 2(c). This is in marked difference from the rigid-airfoil system behavior (see Fig. 2(d)), where three trailing edge vortices suffice to describe the entire trailing edge evolution. In accordance with our problem formulation, the first trailing edge vortex is released in both cases at the initial time
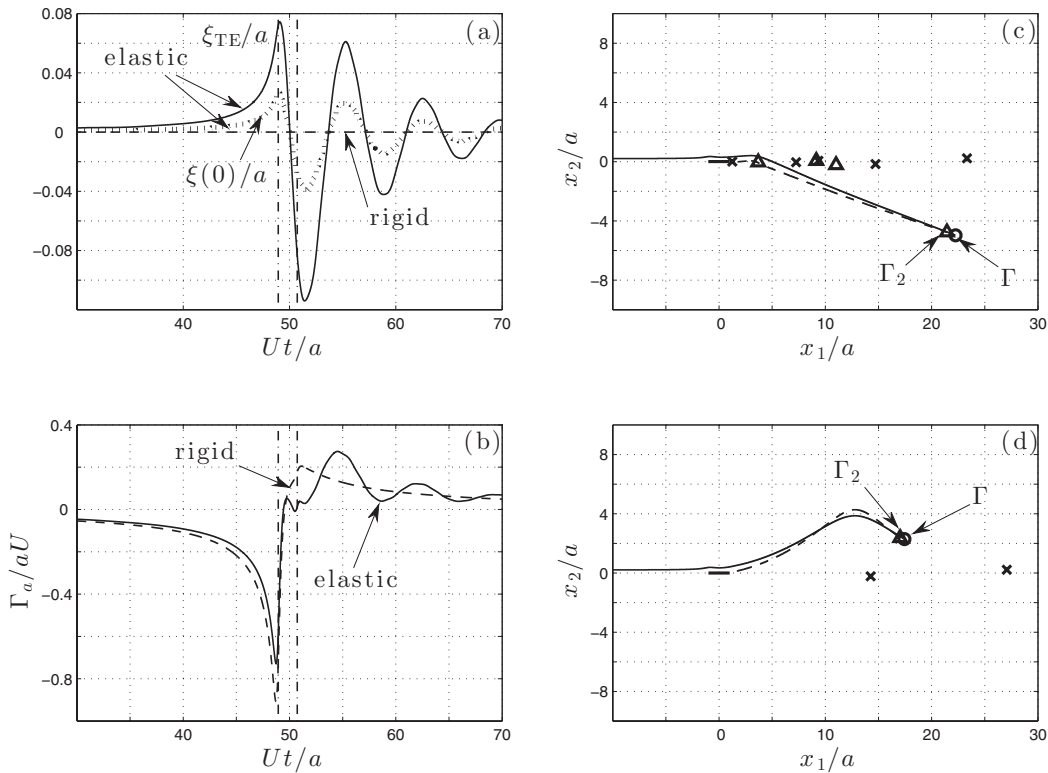
FIG. 2. Near-field dynamics for non-pitching elastic and rigid airfoils: (a) time variations of trailing edge (solid) and mid-chord (dotted) displacements for an elastic airfoil (the dashed line marks the stationary state of the rigid airfoil, for reference); (b) total airfoil circulation for the elastic (solid) and rigid (dashed) airfoils; (c) and (d) vortical-field snapshots for the elastic (Fig. 2(c)) and rigid (Fig. 2(d)) setups at $Ut/a = 70$. In Figs. 2(c) and 2(d), crosses and triangles mark instantaneous trailing edge vortices' locations with positive ($\Gamma_k > 0$) and negative ($\Gamma_k < 0$) circulations, respectively, and circles denote locations of incident vortex. Solid and dashed curves show trajectories of incident vortex Γ and trailing edge vortex Γ_2, respectively. In Figs. 2(a) and 2(b), vertical dashed-dotted lines confine time interval during which the incident vortex passes above the airfoil in the elastic-airfoil setup.

$t = 0$; then, as the vortex passes above the airfoil, the first trailing edge vortex is detached and the release of a second vortex (denoted Γ_2, and opposite in sign to Γ) is initiated. Soon after the incident vortex passes above the trailing edge, the second vortex is subsequently detached, and follows the incident vortex in a "vortex-pair-like" motion (see the solid and dashed trajectories in Figs. 2(c) and 2(d)). From this point on, vortical field evolution differs markedly between elastic and rigid setups: airfoil oscillations induced in the elastic case lead to successive release of opposite-sign trailing edge vortices, whereas the rigid static configuration results in the release of only one additional vortex. In both setups, airfoil circulation vanishes at late times (recovering its initial value), and the release of trailing edge vorticity diminishes accordingly. As will be demonstrated below, the indicated differences in wake topology have a major effect on the acoustic signature of the two systems.

Fig. 3 compares between far-field radiations of elastic and rigid non-pitching airfoils. Focusing on the lift ($\theta = 0$) dipole, Figs. 3(a)–3(c) compare between the separate airfoil motion, incident vortex, and wake sound contributions, respectively, and Fig. 3(d) shows the total acoustic signature of the system. Starting with Fig. 3(d), we note that significant deviation between rigid- and elastic-airfoil signatures starts when the vortex approaches the structure leading edge. At that time, sound amplitude increases considerably in the elastic case (see the sharp maximum in the solid curve at its intersection with the left vertical dashed-dotted line in Fig. 3(d)). In addition, once the vortex has passed above the airfoil trailing edge, oscillatory pressure fluctuations, absent in the rigid-airfoil setup, are radiated by the elastic-airfoil system.
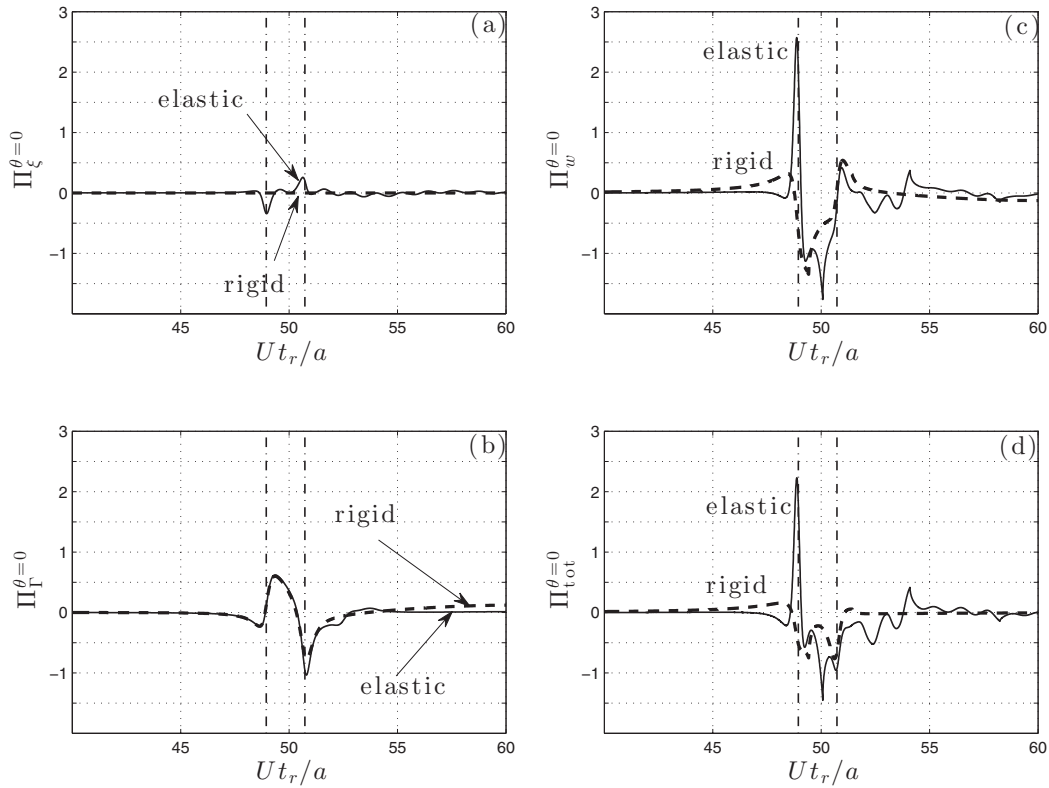
FIG. 3. Far-field radiation for non-pitching elastic (solid lines) and rigid (dashed lines) airfoils in the normal ($\theta = 0$) direction: (a) airfoil motion sound; (b) incident vortex sound; (c) wake sound; (d) total radiation. Vertical dashed-dotted lines confine time interval during which the incident vortex passes above the airfoil in the elastic-airfoil setup.

As observed in Fig. 3(a), the sound induced by direct airfoil motion is relatively weak, while incident vortex sound is nearly unaffected by airfoil elasticity (cf. the solid and dashed lines in Fig. 3(b)). The differences described above between rigid and flexible airfoil signatures therefore originate from the wake sound contribution, shown in Fig. 3(c). Comparing between the vortex and wake noise in the rigid configuration (dashed lines in Figs. 3(b) and 3(c), respectively), we find that wake sound tends to reduce incident vortex noise, leading to a weaker total signal, as was also noted in previous studies of rigid-structure configurations (e.g., Ref. 35). In our discrete wake model, generation of trailing edge vorticity during incident vortex passage above the rigid airfoil accumulates into a single vortex (denoted Γ_2 in Fig. 2), which later on "follows" the incident vortex to form a "silent" vortex pair. However, the additional effect of elasticity results in qualitative changes in the acoustic signature. At leading edge time, the upward bending of the airfoil reduces the distance between the vortex and the trailing edge, causing the vortex interaction with the end-point to become more singular and release larger amount of vorticity. Then, at later times, induced airfoil oscillations lead to successive release of trailing edge vortices, resulting in oscillatory wake sound. It is therefore found that structure elasticity increases noise levels in the passive (non-pitching) setup. As we consider the airfoil response at subcritical conditions, the structure resumes its unperturbed state at late times, where the acoustic far field vanishes.

To characterize the oscillatory behavior of the elastic-airfoil system, Figure 4 presents spectral decompositions of trailing edge deflection and total lift dipole for a non-pitching elastic airfoil. Defining the time Fourier transform of a function F as

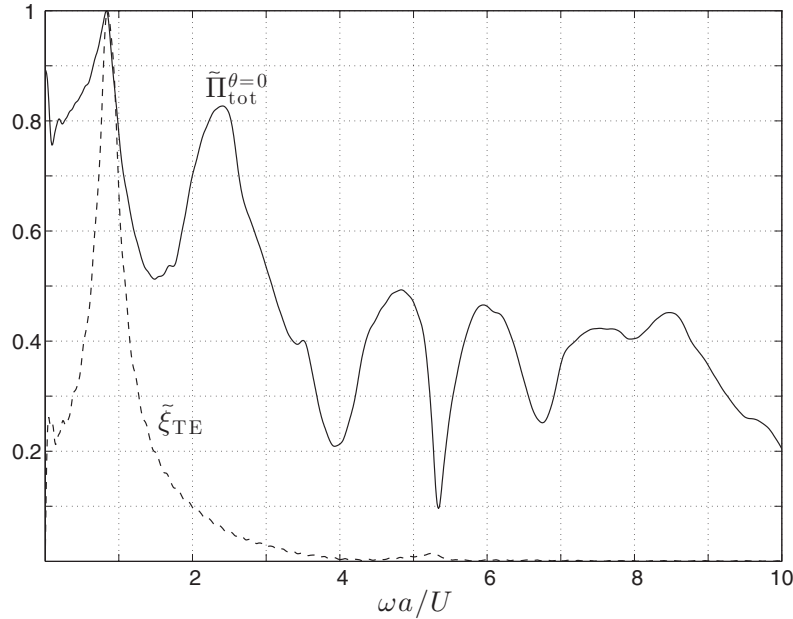$$\widetilde{F}(\bar{\omega}) = \int_{-\infty}^{\infty} F(\bar{t}) \exp(-i\bar{\omega}\bar{t}) d\bar{t}, \tag{36}$$

FIG. 4. Spectral decompositions of far-field radiation in the normal ($\theta = 0$) direction ($\widetilde{\Pi}_{tot}^{\theta=0}$, solid line) and trailing edge displacement ($\widetilde{\xi}_{TE}$, dashed line) for a non-pitching elastic airfoil. Values in each curve are scaled by their respective maximum.

Fig. 4 shows scaled results (normalized by the respective maximum in each curve) for $\widetilde{\xi}_{TE}$ (dashed line) and $\widetilde{\Pi}_{tot}^{\theta=0}$ (solid line). Clearly, we observe that trailing edge motion (representing the motion of the entire airfoil) is dominated by a single frequency, $\bar{\omega}_{res} = \omega_{res}a/U \approx 0.83$, characterizing the late-time oscillations found in Fig. 2(a). The far-field radiation is consequently dominated by the same frequency; in addition, a secondary peak at $\bar{\omega} \approx 3\bar{\omega}_{res}$ is also observed.

Recalling that we focus on a non-actuated airfoil response, it is expected that the motion induced by the incident vortex passage (which can be mathematically described as a propagating delta function, containing the entire spectrum of frequencies) will excite oscillatory airfoil motion at the structure-fluid least stable eigenfrequency. At the present subcritical conditions ($\bar{\mu} = 10$ and $\bar{\alpha} = 1$), this frequency is given by the above value of $\bar{\omega}_{res} \approx 0.83$. A qualitatively similar result was found when studying the linearized problem for a vortex passing above a passive sheet.[21] Yet, a major difference between the two results is in the spectral decomposition of the acoustic field; here, the signal contains a secondary frequency peak, which is missing in the linearized analysis (cf. Fig. 8 in Ref. 21). The relation of this contribution to the nonlinear effect of wake-structure interactions is rationalized below (see Fig. 6).

B. Pitching airfoil

To study the effect of pitching actuation, Figure 5 presents the dynamic and acoustic fields of elastic and rigid airfoils actuated at $\omega_p a/U = 1$, where the vortex residence time above the airfoil approximately equals the mechanical period of pitching. Fig. 5(a) shows trailing edge motion in the elastic case (compared with the sinusoidal motion prescribed in the rigid-airfoil setup) and Fig. 5(b) shows the acoustic signatures of the elastic and rigid airfoils.

Starting with Fig. 5(a), we notice that trailing edge deflections obtained in the elastic airfoil are larger than in the rigid setup, and that the largest amplitudes occur when the vortex passes above the airfoil. We recall that the pitching frequency considered, $\omega_p a/U = 1$, is relatively close to the least stable eigenfrequency of the elastic-airfoil system, $\omega_{res}a/U \approx 0.83$, discussed in Fig. 4. The system therefore amplifies the actuating signal. This, in turn, leads to increased sound levels, as observed from comparison between the dashed and solid curves in Fig. 5(b). At early times, incident vortex sound is negligible, and the total radiation reflects contributions from Π_ξ and Π_w (see Fig. 6(a)).
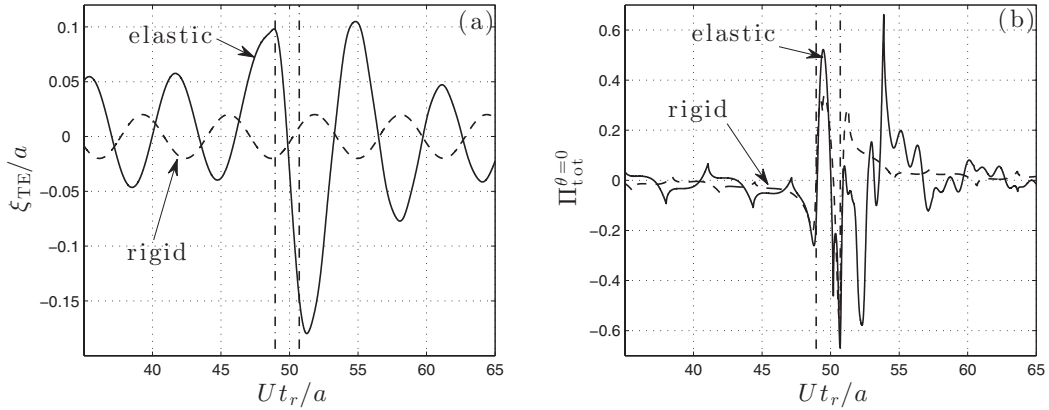
FIG. 5. Near-field dynamics and far-field radiation of elastic (solid lines) and rigid (dashed lines) airfoils pitching at $\omega_p a/U = 1$: (a) trailing edge motion; (b) total far-field radiation in the normal ($\theta = 0$) direction. Vertical dashed-dotted lines confine time interval during which the incident vortex passes above the airfoil in the elastic-airfoil setup.

Both Π_ξ and Π_w are periodic at this stage, reflecting sinusoidal motion of the airfoil and outcome release of trailing edge vortices. Sound amplitude of the elastic airfoil is nevertheless larger than that of the rigid airfoil, owing to the larger magnitudes of motion excited.

When the vortex approaches the airfoil, its interaction with structure end points intensifies, leading to significant variations in Π_Γ, and affecting the airfoil motion and release of trailing edge vorticity. In the rigid airfoil setup this effect is essentially "local," and confined to a short time
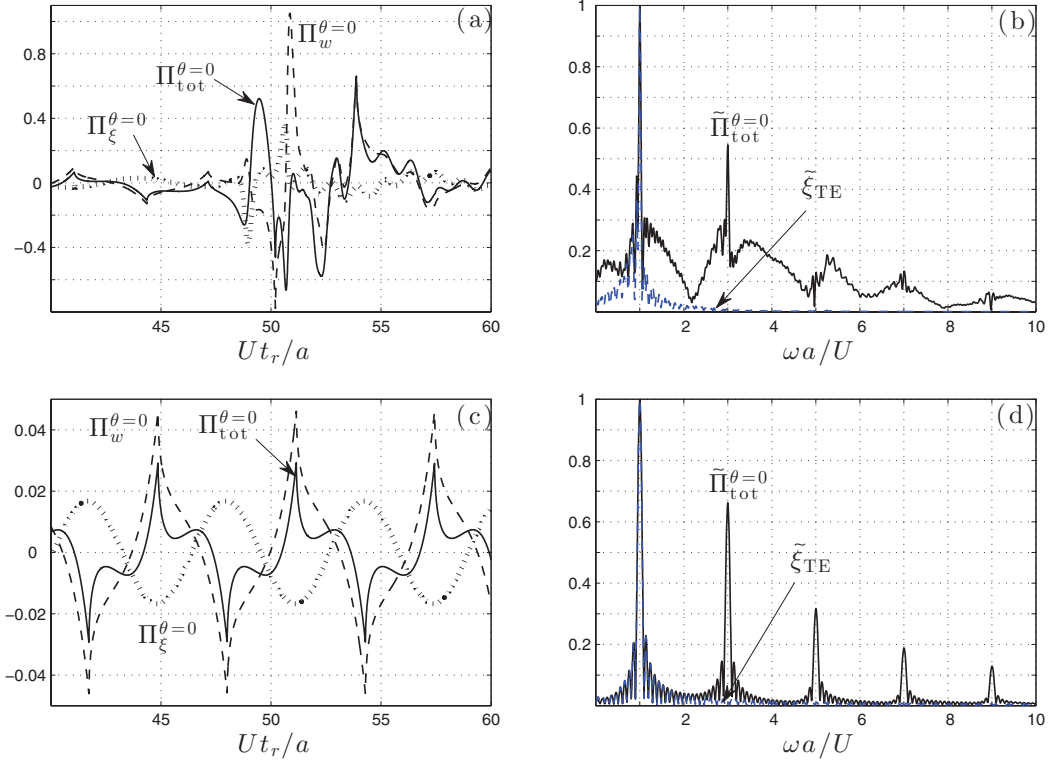

FIG. 6. (a) Pressure components and total far-field radiation in the normal ($\theta = 0$) direction, and (b) spectral decompositions of far-field radiation ($\widetilde{\Pi}_{tot}^{\theta=0}$, solid line) and trailing edge displacement ($\widetilde{\xi}_{TE}$, dashed blue line), for a pitching elastic airfoil at $\omega_p a/U = 1$. (c) and (d) Counterpart results for an actuated elastic airfoil in the absence of an incident vortex ($\Gamma = 0$). Values in each of the curves in Figs. 6(b) and 6(d) are scaled by their respective maximum.

interval after the vortex has passed above the airfoil. However, in the elastic case, airfoil oscillations induced by the vortex add to the periodic pitching signal, and are detected long after the vortex has passed the structure. Remarkably, we observe that the acoustic signature of the elastic airfoil at late times contains a frequency higher than the primary actuation frequency $\omega_p a/U = 1$.

To gain further insight into this behavior, Figure 6 presents a more detailed analysis of the acoustic signal presented in Fig. 5(b). Fig. 6(a) shows separate contributions of airfoil motion noise (Π_ξ) and wake sound (Π_w) to the total lift radiation, and Fig. 6(b) presents time Fourier decompositions (see (36)) of the total radiation and trailing edge motion. For reference, Figs. 6(c) and 6(d) show counterpart results for an actuated elastic airfoil in the absence of incident vortex, i.e., when $\Gamma = 0$, in which structure dynamics is entirely excited by leading edge actuation.

As in the case of a non-pitching airfoil (see Fig. 3), our calculations indicate that total acoustic signature is dominated by wake sound at all times, excluding the time interval of vortex passage above the airfoil. At this time, both structure motion sound and particularly incident vortex noise become significant and affect the total radiation. At leading edge time, total radiation is dominated by incident vortex contribution (not presented here), while at trailing edge time wake sound acts to cancel incident vortex noise and reduce the total radiation. The spectral analysis of the acoustic signal in Fig. 6(b) reveals that, in addition to the dominant $\bar{\omega}_p = \omega_p a/U = 1$ component (being the single component in $\widetilde{\bar{\xi}}_{\text{TE}}$), higher odd multiple harmonics at $\bar{\omega} \approx 3\bar{\omega}_p, 5\bar{\omega}_p, 7\bar{\omega}_p, \ldots$ also exist. This is in qualitative agreement with the appearance of the secondary peak at $\bar{\omega} \approx 3\bar{\omega}_{\text{res}}$ in the Fourier decomposition of the passive-airfoil signature in Fig. 4.

The appearance of higher odd multiple harmonics in the acoustic signal is rationalized in Figs. 6(c) and 6(d), by examining the counterpart problem in the absence of incident vortex. In this case, structure motion and far-field radiation are periodic in time, and the acoustic field is given by the sum of Π_ξ and Π_w contributions, yielding the solid line in Fig. 6(c). Having removed the effect of the incident vortex, the spectral decomposition $\widetilde{\Pi}_{\text{tot}}^{\theta=0}$ in Fig. 6(d) clearly contains $\bar{\omega}_p = 1$ and all its odd multiple harmonics, in descending intensity. Separate decompositions of $\widetilde{\Pi}_\xi$ and $\widetilde{\Pi}_w$ (not presented here) show that wake sound is the main cause for appearance of higher harmonics in the total signature, while airfoil motion noise contributes almost entirely to the fundamental frequency $\bar{\omega}_p = 1$. The periodic wake structure, in turn, contains a sequence of discrete vortices with alternating signs (a pair of opposite-sign vortices released during each heaving period), and the respective pressure fluctuation should therefore satisfy

$$\Pi_w(\bar{t}_r + \bar{T}) = \Pi_w(\bar{t}_r) \text{ and } \Pi_w(\bar{t}_r + \bar{T}/2) = -\Pi_w(\bar{t}_r),$$

with $\bar{T} = 2\pi/\bar{\omega}_p$ denoting the scaled heaving period. Evidently, the second of the two requirements is only satisfied by odd multiples of $\bar{\omega}_p$, and excludes even multiples from the spectrum.

Summarizing the above discussion, it is concluded that at the intermediate value of pitching frequency considered, elastic airfoil sound is dominated by trailing edge wake noise. Following the nonlinear mechanism of wake-airfoil interaction, the radiated wake noise contains not only the fundamental pitching frequency, but also its odd multiples. Practically, this implies that even when the fundamental actuation frequency is below hearing threshold, pitching sound may still be perceived through the higher harmonics radiated by the wake. This finding could not be obtained in previous linear analyses, where the wake was *a priori* described as a mono-harmonic vortex sheet (e.g., Ref. 21).

Figure 7 examines the effect of varying the pitching frequency $\bar{\omega}_p$ on the system dynamic and acoustic behaviors. Towards this end, we introduce the *far-field sound energy* of the system,

$$\mathcal{P}_{\text{acous}}(\bar{t}_r) = \int_0^{2\pi} \Pi_{\text{tot}}^2(\bar{t}_r, \theta) \, d\theta, \tag{37}$$

obtained by integration of the squared total radiation (30) over a circle of radius $|\bar{\mathbf{x}}| \to \infty$, together with the *total integrated sound energy*,

$$\mathcal{P}_{\text{acous}}^* = \int_{\bar{t}_r(\bar{x}_{1\Gamma}=-10)}^{\bar{t}_r(\bar{x}_{1\Gamma}=10)} \mathcal{P}_{\text{acous}}(\tau) \, d\tau, \tag{38}$$
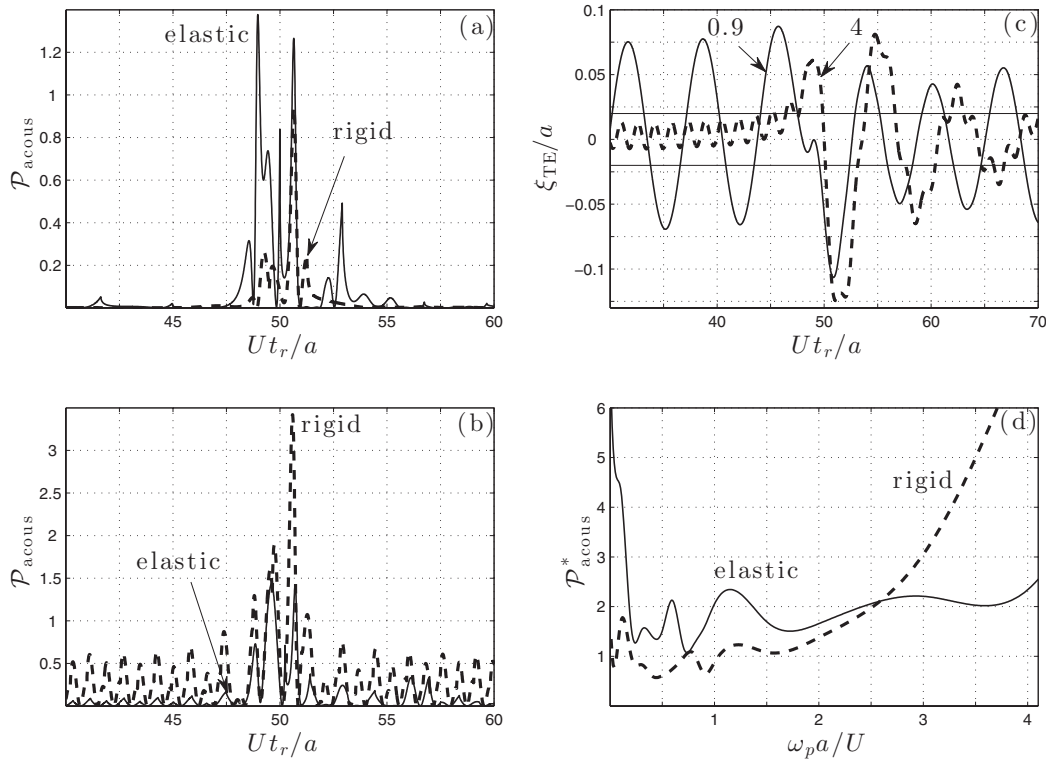
FIG. 7. Effect of pitching frequency on the acoustic far field: (a) and (b) Comparison between sound energy amplitudes of elastic (solid lines) and rigid (dashed) airfoils actuated at $\omega_p a/U = 0.9$ (Fig. 7(a)) and $\omega_p a/U = 4$ (Fig. 7(b)); (c) trailing edge deflections for an elastic airfoil actuated at $\omega_p a/U = 0.9$ (solid line) and $\omega_p a/U = 4$ (dashed line); (d) variation of integrated sound energy amplitude, $\mathcal{P}^*_{\mathrm{acous}}$, with pitching frequency, for elastic (solid curve) and rigid (dashed curve) airfoils. Solid horizontal lines in Fig. 7(c) confine the amplitude of trailing edge motion for a rigid airfoil, for reference.

measuring the total sound radiated by the system at a time interval containing the vortex passage above the airfoil $\left[\bar{t}_r(\bar{x}_{1_\Gamma} = -10) \leq \bar{t}_r \leq \bar{t}_r(\bar{x}_{1_\Gamma} = 10) \right]$. Figs. 7(a) and 7(b) compare between $\mathcal{P}_{\mathrm{acous}}$ for rigid and elastic airfoils actuated at $\omega_p a/U = 0.9$ and $\omega_p a/U = 4$, respectively, and Fig. 7(c) presents the trailing edge displacements of the elastic airfoil in the two cases. Fig. 7(d) shows variation of the integrated sound energy $\mathcal{P}^*_{\mathrm{acous}}$ with pitching frequency for elastic and rigid airfoils.

Focusing on Figs. 7(a) and 7(b), we observe that the rigid airfoil system is much noisier at $\omega_p a/U = 4$ than at $\omega_p a/U = 0.9$, whereas the elastic airfoil retains similar sound levels at both frequencies. Thus, while for $\omega_p a/U = 0.9$ the elastic airfoil is noisier than the rigid (similarly to what has been observed in Fig. 5 for $\omega_p a/U = 1$), the trend is inverted for $\omega_p a/U = 4$, where elasticity is found to attenuate the sound level compared to a rigid setup. This is also reflected in Fig. 7(d), where the value of $\mathcal{P}^*_{\mathrm{acous}}$ is larger for $\omega_p a/U = 0.9$ in the elastic case, and lower for $\omega_p a/U = 4$. According to Fig. 7(d), the change in trends occurs at $\omega_p a/U \approx 2.6$, above which a rigid airfoil becomes noisier. Unlike at low and intermediate actuation frequencies (see Figs. 3(a) and 6(a)), our numerical calculations indicate that at large frequencies, rigid airfoil signature is dominated by airfoil motion sound Π_ξ, whereas Π_Γ and Π_w become relatively small. This results from the $\omega_p^{5/2}$ power dependence of Π_ξ found in (34), leading to high sound levels at high frequencies. In marked contrast, this amplification mechanism is absent in the flexible airfoil setup, where structure elasticity acts to absorb system kinetic energy, and reduce motion amplitudes at actuation frequencies far from system natural eigenfrequency.

As discussed in Fig. 4, the system least stable eigenfrequency for the present $(\bar{\mu}, \bar{\alpha})$ combination is $\omega_{\mathrm{res}} a/U \approx 0.83$. Accordingly, trailing edge motion amplitude is much larger for $\omega_p a/U = 0.9$ than for $\omega_p a/U = 4$ (see Fig. 7(c)). In fact, when ignoring the incident vortex effect, trailing edge deflection for $\omega_p a/U = 4$ for the elastic setup is smaller than for a rigid airfoil (cf. the dashed

curve and two horizontal lines in Fig. 7(c) at early times). Similar behavior is followed at other high actuation frequencies, and reflected through the much larger noise levels radiated by a rigid airfoil when $\omega_p a/U \gg 1$. It can therefore be concluded that, when actuated at frequencies far from (and higher than) system least stable eigenfrequency, structure elasticity reduces radiated sound levels. Consequently, elasticity may be considered as means for developing passive and active methodologies to monitor the acoustic radiation of flapping flight. Further research is required for a specific design of such systems.

IV. CONCLUSION

We studied the acoustic far field of a thin elastic airfoil, subject to low-Mach non-uniform stream flow, and actuated by small-amplitude sinusoidal pitching motion. The near-field fluid-structure interaction problem was analyzed using potential (inviscid) thin-airfoil theory, combined with a discrete Brown-Michael model to describe the evolution of the airfoil trailing edge wake. The leading order dipole-sound signature of the system was analyzed using Powell-Howe acoustic analogy. Compared with the acoustic field of a pitching rigid airfoil, the results demonstrate a two-fold effect of structure elasticity on airfoil acoustic field: at actuation frequencies close to the system least stable eigenfrequency, elasticity amplifies airfoil motion amplitude and associated sound levels; however, at frequencies distant from this eigenfrequency, structure elasticity acts to absorb system kinetic energy and reduce acoustic radiation. In the latter case, and with increasing pitching frequency ω_p, we found the rigid-airfoil setup to be significantly noisier than the elastic airfoil, owing to an $\omega_p^{5/2}$ increase of its motion-induced noise component. In contrast with rigid airfoil signature, our calculations indicate that wake sound contribution to elastic airfoil radiation is significant for all ω_p. This contribution contains, in addition to the fundamental pitching frequency, its odd multiple harmonics, which result from nonlinear interactions between the airfoil and the wake.

The present contribution has applied sinusoidal pitching together with a propagating line vortex to model flapping flight actuation and incoming flow non-uniformity. Yet, our numerical scheme can be easily generalized to consider the system response to arbitrary (small-amplitude) actuation or any distribution of incoming vorticity. In this context, the present choice of sinusoidal actuation can be considered as a single Fourier component of a more general input signal, and the single incident line vortex model can be replaced by a more complex vortical non-uniformity. The near-field interaction of a thin sheet with a vortex street distribution has been studied by Alben,[19] who focused on conditions where vortex street dynamics are unaffected by structure motion. Full coupling between fluid and body motions is therefore yet to be investigated, and can be readily accounted for using the present scheme. We leave this extension for a later discussion.

Perhaps the main finding of the present study is in demonstrating that airfoil elasticity, when coupled with nonlinear fluid-structure interaction forcing, has a significant effect on the system acoustic radiation, both in terms of sound amplitude and frequency characteristics. This suggests elasticity as a possible means for future development of passive and active noise control methodologies. Further research is required to follow this route for an applicative design of such systems.

[1] M. P. Païdoussis, *Fluid-Structure Interaction: Slender Structures and Axial Flow* (Academic, London, 1998), Vol. 1, 572 pp.
[2] M. J. Shelley and J. Zhang, "Flapping and bending bodies interacting with fluid flows," Annu. Rev. Fluid Mech. **43**, 449–465 (2011).
[3] C. Eloy, C. Souilliez, and L. Schouveiler, "Flutter of a rectangular plate," J. Fluids Struct. **23**, 904–919 (2007).
[4] W. X. Huang and H. J. Sung, "Three-dimensional simulation of a flapping flag in a uniform flow," J. Fluid Mech. **653**, 301–336 (2010).

[5] J. C. Liao, D. N. Beal, G. V. Lauder, and M. S. Triantafyllou, "Fish exploiting vortices decrease muscle activity," Science **302**, 1566–1569 (2003).

[6] Y. Watanabe, S. Suzuki, M. Sugihara, and Y. Sueoka, "An experimental study of paper flutter," J. Fluids Struct. **16**, 529–542 (2002).

[7] J. J. Allen and A. J. Smits, "Energy harvesting eel," J. Fluids Struct. **15**, 629–640 (2001).

[8] M. S. Howe, *Acoustics of Fluid-Structure Interactions* (Cambridge University Press, Cambridge, 1998), 571 pp.

[9] L. Huang, "Mechanical modeling of palatal snoring," J. Acoust. Soc. Am. **97**, 3642–3648 (1995).

[10] H. C. Bennet-Clark, "Acoustics of insect song," Nature **234**, 255–259 (1971).

[11] J. Sueur, E. J. Tuck, and D. Robert, "Sound radiation around a flying fly," J. Acoust. Soc. Am. **118**, 530–538 (2005).

[12] Y. Bae and Y. J. Moon, "Aerodynamic sound generation of flapping wing," J. Acoust. Soc. Am. **124**, 72–81 (2008).

[13] L. Tang and M. P. Païdoussis, "On the instability and the post-critical behaviour of two-dimensional cantilevered flexible plates," J. Sound Vib. **305**, 97–115 (2007).

[14] S. Alben and M. J. Shelley, "Flapping states of a flag in an inviscid fluid: bistability and the transition to chaos," Phys. Rev. Lett. **100**, 074301 (2008).

[15] S. Michelin, S. G. Llewellyn Smith, and B. J. Glover, "Vortex shedding model of a flapping flag," J. Fluid Mech. **617**, 1–10 (2008).

[16] S. Michelin and S. G. Llewellyn Smith, "Resonance and propulsion performance of a heaving flexible wing," Phys. Fluids **21**, 071902 (2009).

[17] S. Alben, "Simulating the dynamics of flexible bodies and vortex sheets," J. Comput. Phys. **228**, 2587–2603 (2009).

[18] A. Manela and M. S. Howe, "The forced motion of a flag," J. Fluid Mech. **635**, 439–454 (2009).

[19] S. Alben, "Passive and active bodies in vortex-street wakes," J. Fluid Mech. **642**, 95–125 (2010).

[20] A. Manela and M. S. Howe, "On the stability and sound of an unforced flag," J. Sound Vib. **321**, 994–1006 (2009).

[21] A. Manela, "Sound generated by a vortex convected past an elastic sheet," J. Sound Vib. **330**, 416–430 (2011).

[22] A. Manela, "Vibration and sound of an elastic wing actuated at its leading edge," J. Sound Vib. **331**, 638–650 (2012).

[23] A. Manela and T. Miloh, "Forced motion and acoustic radiation of an elastic cylinder in axial flow," J. Sound Vib. **331**, 3544–3557 (2012).

[24] M. S. Howe, *Theory of Vortex Sound* (Cambridge University Press, Cambridge, 2003), 216 pp.

[25] H. Abou-Hussein, A. DeBenedictis, N. Harrison, M. Kim, M. A. Rodrigues, F. Zagadou, and M. S. Howe, "Vortex-surface interaction noise: a compendium of worked examples," J. Sound Vib. **252**, 883–918 (2002).

[26] S. Alben, "The attraction between a flexible filament and a point vortex," J. Fluid Mech. **697**, 481–503 (2012).

[27] A. Manela and L. Huang, "Point vortex model for prediction of sound generated by a wing with flap interacting with a passing vortex," J. Acoust. Soc. Am. **133**, 1934–1944 (2013).

[28] C. E. Brown and W. H. Michael, "Effect of leading edge separation on the lift of a delta wing," J. Aeronaut. Sci. **21**, 690–706 (1954).

[29] C. E. Brown and W. H. Michael, "On slender delta wings with leading-edge separation," NACA Technical Note No. 3430, 1955.

[30] S. Michelin and S. G. Llewellyn Smith, "An unsteady point vortex method for coupled fluid-solid problems," Theor. Comput. Fluid Dyn. **23**, 127–153 (2009).

[31] X. Dai, X. Jing, and X. Sun, "Vortex shedding and its nonlinear acoustic effect occurring at a slit," AIAA J. **49**, 2684–2694 (2011).

[32] X. Dai, X. Jing, and X. Sun, "Discrete vortex model of a Helmholtz resonator subjected to high-intensity sound and grazing flow," J. Acoust. Soc. Am. **132**, 2988–2996 (2012).

[33] M. C. A. M. Peters and A. Hirschberg, "Acoustically induced periodic vortex shedding at sharp edged open channel ends: simple vortex models," J. Sound Vib. **161**, 281–299 (1993).

[34] M. S. Howe, "Emendation of the Brown & Michael equation, with application to sound generation by vortex motion near a half-plane," J. Fluid Mech. **329**, 89–101 (1996).

[35] M. S. Howe, "The influence of vortex shedding on the generation of sound by convected turbulence," J. Fluid Mech. **76**, 711–740 (1976).